Growth pyramids on Si(111) facets: A CVD and MBE study

J. van Wingerden, R. H. van Aken, Y. A. Wiechers, P. M. L. O. Scholte, and F. Tuinstra
Department of Applied Physics and Delft Institute for Microelectronics and Submicron Technology, Delft University of Technology, Lorentzweg 1, 2628 CJ Delft, The Netherlands
(Received 9 May 1997)

The morphology of growth pyramids on Si(111) facets has been studied with an atomic force microscope. These facets with pyramids are formed upon chemical vapor deposition (CVD) growth on a hemispherical substrate. Spiral as well as concentric step edge patterns have been observed on the growth pyramids. Based on the step edge patterns the origin of the pyramids is attributed to different types of dislocations. Step edge patterns indicate that growth during CVD is governed by step edge processes and that surface diffusion is not rate limiting. The completely different growth mechanism of molecular-beam epitaxy (MBE) is illustrated by MBE overgrowth of a silicon layer on top of the CVD layer. MBE growth parameters have been studied by comparing the growth pyramid morphology with simulation results. [S0163-1829(98)04812-7]

I. INTRODUCTION

The atomic-scale mechanisms involved in crystal growth strongly depend on the growth circumstances and crystallographic orientation of the substrate. Direct observation of the atomic-scale growth processes is often impossible, but the morphology of the layers formed during growth is intimately related to the details of the growth process. Therefore, analysis of as-grown layers is a major tool in the study of growth mechanisms. The characteristic features observed in the step edge patterns on the as-grown surfaces provide information about basic growth processes like surface diffusion, island nucleation, and growth at step edges.

Hemispherical substrates are ideally suited for studying growth processes. Surfaces with different orientations and step densities all experience the same growth conditions and thus can be compared directly. This has for example been demonstrated by Gardeniers for the case of homoepitaxial growth of silicon by chemical vapor deposition (CVD).[1] There is also another important reason for using hemispherical substrates in epitaxial growth studies. On these substrates the exact low index orientations are always available and, therefore, facets can develop. Because of inaccuracies in the preparation, flat substrate surfaces can never be prepared exactly in a low index orientation. The resulting step density will influence the growth mode and thus hide the processes related to the growth on terraces. In this study we focus on the (111) facets formed during homoepitaxial growth of Si by CVD. These facets are not flat, but contain three-sided growth pyramids (see Fig. 1). Because the pyramids are very shallow with sideplanes deviating less than 0.5° from the (111) facet, these sideplanes must be considered as vicinal (111) planes. The number of growth pyramids differs strongly for the individual facets, but no (111) facets without three-sided pyramids have been observed. Similar three-sided pyramids have been reported earlier for Si(111) (Refs. 2–5) as well as for diamond (111) (Refs. 6–8) surfaces. The origin of these pyramids was generally attributed to screw dislocations although the formation of defect-free pyramids was also claimed.[2] In the latter case their formation should be intrinsically related to the growth on facets. For the growth of boron containing diamond films, scanning tunneling microscopy (STM) observations have demonstrated the existence of growth spirals generated by dislocations.[9]

Here, we first establish the nature of the pyramids as revealed by atomic force microscope (AFM) images of the individual step edges (see Sec. III). Subsequently, we study the relation between the observed growth morphologies on the (111) facets and the growth mechanisms that are responsible for them. Section IV discusses the features of the step edge patterns observed for the CVD grown layer as well as their implications for the growth process. For molecular-beam epitaxy (MBE) growth a strongly different surface morphology is expected due to the different nature of its growth mechanism. Direct MBE growth on the as-prepared hemispheres as performed for CVD growth does not yield

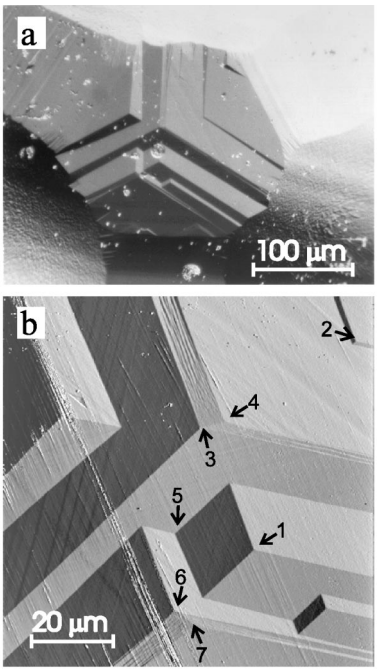

FIG. 1. Nomarski microscope image (a) of a single (111) facet with a number of shallow growth pyramids formed during CVD growth. AFM deflection image (b) ($90\times90\ \mu m^2$) of the central part of the (111) facet in (a). Site 5 indicates a valley, the other sites correspond to pyramid tops.

any indication of facet formation. Obviously the initial surface irregularities on the substrate are too large to be overcome by the MBE growth mechanisms. This problem is solved by performing the MBE growth on top of a CVD grown layer. The pronounced changes in the morphology of the pyramids due to the overgrowth of the 2.9-μm-thick MBE layer is shown in Sec. V. In the next section computer simulations of the MBE growth process are used to relate the influence of specific growth parameters to the experimentally observed morphology.

II. EXPERIMENTS

Monocrystalline hemispherical Si substrates with a 5-mm radius have been produced by grinding and polishing. Subsequently, the top layer was removed by isotropic etching with a 1:8 solution of HF (40%) and HNO_3 (65%).[10] In this manner the defect density at the surface of the hemisphere is reduced.

With CVD, a 10-μm-thick epitaxial layer is grown on the hemisphere. Growth is performed with SiH_2Cl_2 in H_2 at a pressure of 150 Torr and a temperature of 975 °C; the growth rate is 0.2 μm/min. On one of the substrates an MBE layer is grown on top of the CVD layer. This layer, which has a thickness of 2.9 μm on the (111) facet, is deposited at a rate of 0.6 μm/h at 900 °C.

The details of the surface structures on the (111) facet resulting from CVD and the effects of subsequent overgrowth with MBE have been studied with AFM. Two AFM image types have been used. The height images are used to measure the slopes and height differences. We also use deflection images, which represent the error signal in the feedback loop of the constant force mode. The error signal is proportional to changes in the height of the surface, i.e., it represents the derivative of the surface height profile. This deflection signal is better suited for illustrating the shallow features like step edges. Both types of images are measured with the tip in contact with the sample, in a constant force mode.

III. ORIGIN OF THE GROWTH PYRAMIDS

As shown in the large scan area image in Fig. 1(b) we have been able to locate the center part of the facet on the hemisphere under the AFM. Even though the surface is covered by a thin native oxide layer, small scan area AFM images reveal individual step edges. These step edge structures directly demonstrate the nature of the growth pyramids as shown in Fig. 2(a) for the pyramid top indicated as number 1 in Fig. 1(b). The step edge spiral on this pyramid clearly demonstrates the presence of a dislocation, ending exactly at the top of the pyramid. The Burgers vector of this dislocation is not necessarily perpendicular to the surface. It is sufficient to have a component perpendicular to the surface terraces. This will result in a step edge with a step height equal to this perpendicular component. The height of the step edges on the side planes of the growth pyramids is determined using the vicinal angle measured from the height image and the step density measured from the corresponding deflection image. A step height of $0.31+/-0.04$ nm was measured for all side planes of the different pyramids. This is in very good agreement with the elementary step height on the Si(111)

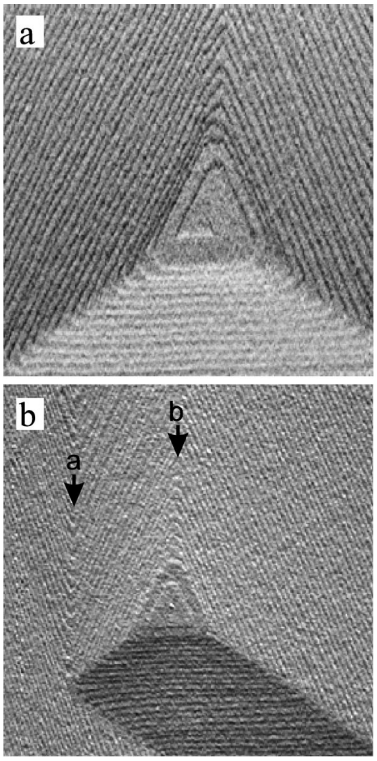

FIG. 2. AFM deflection images of growth pyramid tops showing (a) the step edge spiral on pyramid top 1 and (b) the concentric triangular step pattern on pyramid top 2. The regions *a* and *b* exhibit concave and convex step edge structures, respectively. Note that the images are rotated with respect to Fig. 1(b). Image sizes: (a) 2×2 μm^2, (b) 4×4 μm^2.

plane, which is 1/3 [111] because the cubic unit cell of the diamond lattice contains three (elementary) double layer distances in the [111] direction. Thus, the Burgers vector of the dislocation generating the growth pyramid in Fig. 2(a) has a component along [111] equal to 1/3 [111]. Burgers vectors of perfect dislocations in the diamond lattice have to be the shortest translation vector of the lattice, i.e., 1/2 [110].[11] This Burgers vector's component along [111] is indeed 1/3 [111]. The exact nature of the dislocation i.e., whether it is of the screw type, edge type, or mixed type cannot be determined, since the direction of the dislocation line inside the crystal cannot be deduced from observations of the surface of the facet only.

We also observed growth pyramids with a step edge structure different from that of pyramid 1. Figure 2(b) demonstrates the observation of a concentric triangular step edge structure at the top of pyramid 2. The concentric step edge structure indicates that if the pyramid contains one or more dislocations, the net Burgers vector does not have a component perpendicular to the (111) terrace. As proposed earlier,[12–15] dislocations with a Burgers vector parallel to the surface also generate growth steps. The mechanism for generating these steps is related to the dissociation of the dislocation in two partial dislocations[13–15] (e.g., $1/2[1\bar{1}0] \rightarrow 1/6[2\bar{1}1]+1/6[1\bar{2}\bar{1}]$). The resulting partial dislocations have Burgers vector components, which are perpendicular to the (111) terrace. These perpendicular components have opposite signs. Due to the energy involved in the creation of the stacking fault in between the partial dislocations, their separation is limited. A splitting at the surface of the order of

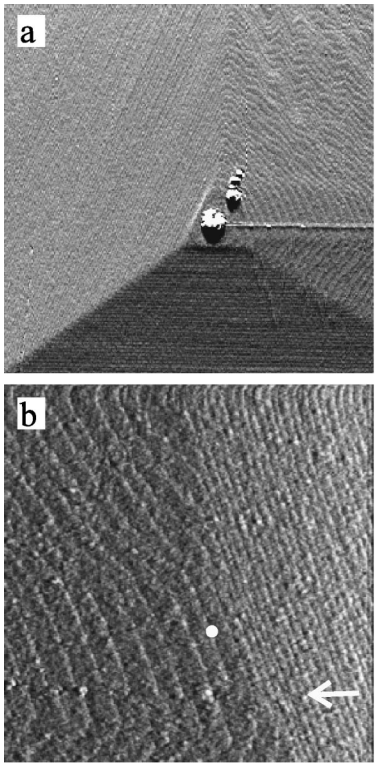

FIG. 3. AFM deflection images of the step edge patterns at pyramid top 3 in (a) and top 4 in (b). (The images are rotated over a small angle with respect to Fig. 2.) In (b) an extra step edge, indicated with a bright dot, emerges at the end of the defect line, the vertical position of which is indicated with an arrow. At the left-hand side of the step edge emergence point, the defect line visibly disturbs the surface structure. To the right, in the region of the arrow, no disturbance of the step edges is observed. Image sizes: (a) $5\times5\ \mu m^2$, (b) $2\times2\ \mu m^2$.

100 nm has been observed.[15] The sharp point in the middle of the pyramid's top terrace in Fig. 2(b) indicates the presence of such a pair of partial dislocations. An upper limit for its size, which has been determined from larger magnification images, indicates a splitting of the two partials of at most 50 nm. Further details of the formation of steps at this dislocation center cannot be obtained due to the presence of the native oxide on the surface and the small separation of the two partial dislocations.

A third type of step edge structure is observed on the double pyramid, the tops of which are indicated as 3 and 4 in Fig. 1(b). Two side planes of pyramid 3 have an equidistant pattern of straight step edges [see Fig. 3(a)]. The remaining part exhibits an irregular step edge pattern, but it does not contain an obvious step edge source. The step edges of this pyramid seem to form concentric loops. However, a straight defect line starting at the center of the pyramid is disturbing the terraces and the step edges. This line is about 6.5 μm long and connects the pyramid tops 3 and 4. The defect causing the straight line at the surface is determined by the crystal structure, as it is aligned along [110]. The step edge structure at the other end of the defect line on pyramid top 4 is shown in Fig. 3(b). Here, we observe the generation of an additional step edge by a dislocation emerging at the surface. Furthermore, the step edges are not continuous at the defect line. Because of the length of the defect line interconnecting the two pyramid tops and the different structures at the two tops, this cannot be a widely dissociated single dislocation with Burgers vector 1/2 [110]. It should have a more complex dislocation source, the exact nature of which cannot be determined from its appearance at the surface. A macroscopically similar structure is formed by the tops 6 and 7 in Fig. 1(b). A microscopic image of its step structure could not be obtained due to the mechanical damage of the surface near these tops.

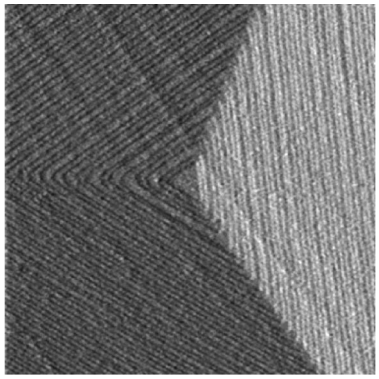

FIG. 4. AFM deflection image of the step edge pattern at the valley in site 5. Image size: $3\times3\ \mu m^2$.

IV. CVD GROWTH FEATURES

Growth from SiH_2Cl_2 involves diffusion through the gas phase, adsorption on the terrace, diffusion over the terraces to step edges and, finally, the attachment of new growth units to these step edges. During these processes the molecule dissociates in a number of reaction steps, finally leaving a single Si atom attached as the growth unit.

Under standard CVD conditions the diffusion length of the adsorbed species is much larger than the terrace length.[16] This fact is nicely demonstrated by the sharp corners in the step edges at the intersections of the pyramid's side planes (see, e.g., Fig. 2). Diffusion limitations would have caused these corners to be heavily rounded off. The sharp corners also indicate that the growth rate strongly depends on the orientation of the step edge. No significantly different growth rate is observed for concave and convex cusps in the step edge. This is especially evident for the two types of corners indicated with *a* and *b* in Fig. 2(b). Similarly, step edges in the valley, shown in Fig. 4, also exhibit sharp corners. Thus, the step edge energy is so highly anisotropic that even reentrant corners remain sharp, in spite of their higher sticking probability.

Another interesting feature is the narrow terrace width distribution, yielding a regular step edge pattern with terrace widths of about 45 nm on all side planes of the pyramids. Therefore, the activity of the step edge sources, having different dislocation stuctures, should be quite similar for all pyramids. The slightly larger terrace immediately at the top of the pyramid or at the bottom of a valley does not seem to cause a substantial disturbance of the terrace widths in its neighborhood. The transition area between the side planes of the two pyramid tops 3 and 4 exhibits much larger terraces, exceeding a width of 100 nm. As Fig. 3(b) shows, the transition between the regions with low and high step densities is

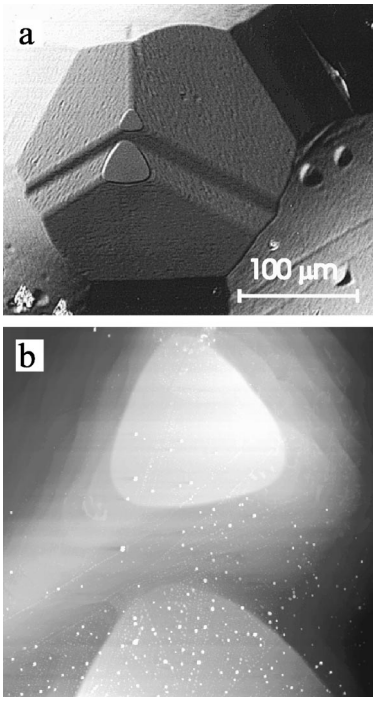

FIG. 5. Nomarski microscope image (a) of a (111) facet after overgrowth with MBE. AFM height image (b) of the smaller of the two facets on top of the growth pyramids in (a). The small white spots are due to contamination on the surface. Image size: $40\times40\ \mu m^2$.

abrupt, but without the formation of a step bunch. The form of this transition indicates that the growth rate at the step edges is not limited by the amount of growth species absorbed on the terraces adjacent to the step edge. This indicates a very large supersaturation on the terraces and/or substantial diffusion across the step edges.

V. MBE GROWTH FEATURES

MBE growth on top of the CVD layers leads to changes in the surface morphology. Here, we again focus on the effects observed for the (111) orientation. The most pronounced feature observed after MBE growth on top of the CVD layer is the formation of a small flat facet on top of the growth pyramids. This is demonstrated in the Nomarski microscope photo in Fig. 5(a), which shows a (111) facet with two growth pyramids. A second important difference between the morphology of the MBE top layer and the CVD layer is the rippled structure on the side planes of the growth pyramids. A third difference is observed at the intersection of the side planes. After CVD this intersection is even on the atomic scale sharply visible [see Figs. 2(a,b)]. During MBE the intersection has broadened strongly, so that it appears as a broad band in the Nomarski microscope image. The broadening is induced by diffusion effects. This diffusion effect also causes the corners of the small facets on top of the pyramids to be rounded off. Finally, MBE overgrowth did not yield a measurable increase in the size of the original (111) facet. On the other hand, we observed in another experiment that deposition of a 5-μm CVD layer on top of a 10-μm CVD layer increases the facet size with about 80%. This is consistent with the orientation independence of MBE growth in comparison with CVD growth.[16]

AFM measurements on the (111) facet shown in Fig. 5(a) have been used to characterize the structures quantitatively. Fig. 5(b) shows a height image of the smaller of the two faces on top of the growth pyramids together with part of the larger one. The white spots in the image are caused by contamination on the surface and are not due to the growth process. The top facets are very flat with a vicinal angle smaller than 0.05°. This means that the top faces are exact (111) terraces or contain only a low density of step edges. No step edges have been observed on the top faces, but detecting them is difficult due to the large surface area and the presence of contamination. Figure 6(a) shows a deflection image of part of the top face with the rippled structure on the pyramid's side plane. Figure 6(b) shows a cross section along the line *A*-*B* in Fig. 6(a). The height profile clearly shows the presence of a high step bunch at the edge of the small (111) facet on top of the pyramid. The ripples on the side plane are formed by smaller step bunches. They seem to be larger close to the edge of the top face [see Fig. 6(b)]. The first step bunch next to the edge of the top face generally has a height that is about 25–30% of the bunch forming the edge. Figure 6(c) gives a detailed height profile of the edge of the larger of the two top faces in Fig. 5(a). It shows that the lateral width of the step bunch is about 0.5 μm. A height difference of about 30 nm on a lateral width of 0.5 μm yields an average terrace width of 5 nm for the terraces in the step bunch. Thus the step bunch can still be considered as a (111) face with a large vicinal angle. The ratio between the diameter of the top face and the height of the step bunch at its edge is approximately 1000 for both the small and the large top facets. At the corners of the top facets a smaller step height is measured. At these places the height of the bunch is reduced

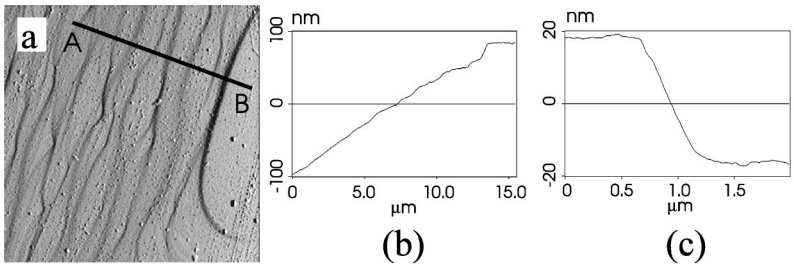

FIG. 6. (a) AFM deflection image ($20\times20\ \mu m^2$) of part of the smaller facet and the step bunch pattern on the side plane. (b) Cross section showing average height profile of a 2-μm-wide area along the line *A*-*B* indicated in (a). (c) Height profile of the step bunch at the edge of the larger facet on the growth pyramid top in Fig. 5(a).

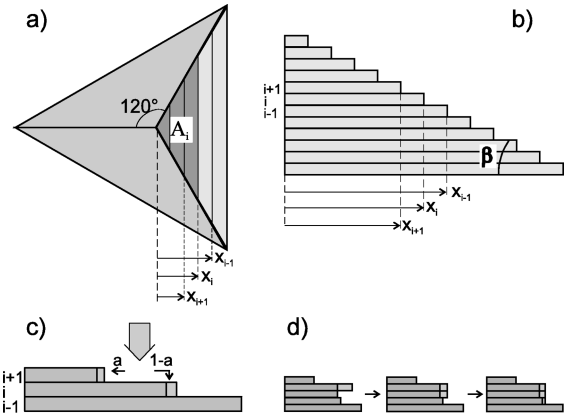

FIG. 7. Schematic top view (a) and cross section of one side plane (b) of the growth pyramid. The Schwoebel parameter, a, models the effect of the asymmetric sticking probability, as drawn in (c). Overhangs created during the simulation are removed in the manner shown in (d).

because the steps in the lower part of the bunch have split off.

Several of the above mentioned features will be used in the next section for comparison with results of numerical simulations.

VI. MBE GROWTH MODEL

The influence of two important growth parameters on the form of the growth pyramid after MBE growth has been simulated using a continuum model. One parameter determines the rate at which new terraces nucleate on the upper terrace of the growth pyramid. Due to the high elastic strain near the dislocation core, the probability for sticking adatoms to step edges is smaller near the core than far away from it. This determines the rate at which new layers are formed. In the simulation this has been modeled by creating new terraces on top of the pyramid after a minimum number of growth units has accumulated on the upper terrace. The other growth parameter determining the morphology of the growth pyramid is the so-called Schwoebel parameter.[17] This parameter describes the asymmetric sticking probability for growth units arriving at step edges from the upper and the lower terrace, respectively. It determines how fluctuations in the step edge positions propagate along the step edge train. Preferential attachment from the upper terrace leads to an instability causing step bunching. On the other hand, preferential sticking from the lower terrace stabilizes an equidistant step pattern. Nucleation of islands on the terraces also gives the effect of increasing the incorporation of material from the lower terrace. This contribution can be included in an effective Schwoebel parameter. It shows that growth by island nucleation leads to a stabilization of an equidistant step edge pattern.[9]

Simulations have been performed, starting from the structure indicated schematically in Figs. 7(a,b). The evolution of the atomic layer areas on one of the three pyramid sides is calculated from:

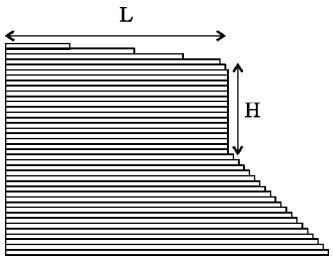

FIG. 8. Typical simulation result showing the cross section of one of the three pyramid side planes. A top face with a low density of steps, a step bunch, and a sideplane can be distinguished. The length of the top face, L, and the corresponding height of the step bunch at its edge, H, are used to characterize the structure.

$$\frac{dA_i}{dt} = C[(1-a)(A_i - A_{i+1}) + a(A_{i-1} - A_i)], \qquad (1)$$

where the area A_i and the effective Schwoebel parameter a are defined in Figs. 7(a), and 7(c), respectively. The proportionality constant C represents the growth rate. The position of the step edge, x_i, can be calculated from the corresponding areas A_i using

$$x_i = \sqrt{\frac{A_i}{\sqrt{3}}}. \qquad (2)$$

The time evolution of A_i according to Eq. (1) may lead to overhangs, which is physically incorrect. In these cases the step edge positions are corrected by redistributing the overhang volume over the step edges below it in the manner shown in Fig. 7(d).

Part of the material deposited on the upper terrace is not incorporated in a step edge, but is accumulated on that terrace. For simplicity we assume the fraction of deposited material that is accumulated on the top terrace to be equal to the Schwoebel parameter a. A new terrace is generated on top of the growth pyramid if the accumulated amount of growth units on the upper terrace exceeds a critical surface area A_c.

The initial structure used in the simulations has equal terrace widths T. The influence of an upper terrace with an initially larger size has been neglected as its influence gradually fades away during the evolution of the structure. In most cases a relatively flat top face, bordered by a step bunch, develops during the simulation [see Fig. 8]. Characteristic features like the size of the top face, L, and the height of the step bunch, H, are used for comparing the simulation results to the measured form of the growth pyramid. In the simulations, we found a constant ratio H/L. This ratio is determined by the geometry of the pyramid, according to

$$H/L = \tfrac{1}{3} \tan \beta, \qquad (3)$$

where β is the vicinal angle of the pyramid's side plane. In the results presented hereafter, we have simulated the growth of a layer with total thickness equal to that grown in the MBE experiment (i.e., 9200 layers with a thickness of 0.31

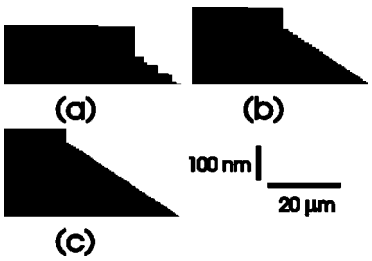

FIG. 9. Sideplane cross sections from simulations with different Schwoebel parameters, a: $a=0.40$ in (a), $a=0.45$ in (b), and $a=0.50$ in (c), respectively. The critical surface area $A_c=35\ \mu\text{m}^2$.

nm). All results scale linearly with the initial terrace size, T. Numerical results, e.g., for the size of the top face, have been calculated with $T=45$ nm.

The Schwoebel parameter, a, has the most pronounced influence on the form of the growth pyramid, as demonstrated by the simulation results in Fig. 9. Higher values of the Schwoebel parameter result in a decrease in the size of the top face and a smaller magnitude of the ripples on the sideplane. A Schwoebel parameter of 0.40 results in a rough sideplane, while the irregularities on the sideplane are already fairly small for $a=0.50$. For Schwoebel parameter values above 0.50, the ripples on the sideplane rapidly vanish, as demonstrated by the simulation results for $a=0.50$ and $a=0.55$ in Fig. 10. These results are in accordance with the expected stabilization of an equidistant step edge pattern in case of preferential sticking from the lower terrace. Not only the sideplane itself, but also the transition to the sideplane at the bottom of the step bunch becomes smooth for $a=0.50$ and above. The flat top face does not vanish for $a>0.5$, as the barrier for nucleating a new island (modeled by the critical surface area A_c) yields an increased contribution from the upper terrace to the first step edge.

Based on the experimentally observed sideplane morphology, the Schwoebel parameter is estimated to fall in the range 0.40–0.50 for the MBE growth conditions used in the experiment. For this parameter range the length of the top face, L, varies from 35 to 17 μm, which is the same order of magnitude as the experimentally observed size. It should be noted, however, that the length of the top face not only depends on the Schwoebel parameter, but also on the critical surface area A_c. For the simulation results mentioned above, a critical surface area $A_c=35\ \mu\text{m}^2$ has been used. Decreasing the value of A_c yields smaller top surfaces with a higher slope. This is evidenced, for example, by the simulation result shown in Fig. 11(b), which has been obtained with a 100 times smaller value of A_c. The size of the top face is reduced with a factor 3.6 and the terrace length on the top face with a factor 10. The corresponding slope of the top surface is now 0.05°, which is the experimentally determined upper limit for this slope.

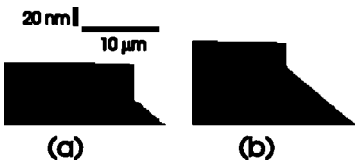

FIG. 10. Simulated sideplane cross sections with $A_c=35\ \mu\text{m}^2$ shown at a larger scale for $a=0.50$ (a) and $a=0.55$ (b).

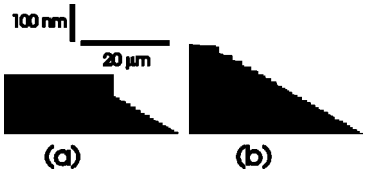

FIG. 11. Simulated sideplane cross sections with $A_c=35\ \mu\text{m}^2$ (a) and $A_c=0.35\ \mu\text{m}^2$ (b) for the same value of the Schwoebel parameter, $a=0.45$.

The dependence of the top surface slope on the critical surface coverage suggests that we can determine a lower limit for the critical surface coverage needed for terrace nucleation. However, for $a=0.45$, A_c amounts to 27% of the upper terrace area upon nucleation of the new terrace. A much smaller critical surface area would be expected. Furthermore, the surface coverage required for the nucleation does not change with the reduction of A_c by the factor 100. This paradoxical result can be understood by realizing that in the simulation model A_c is a terrace size independent value, which just determines when a new terrace is generated. Reducing A_c yields a higher terrace generation rate and thus a larger slope on the pyramid's top face. The surface coverage upon nucleation changes with the value of the Schwoebel parameter (from 23% at $a=0.40$ to 31% at $a=0.50$), but remains very high. For obtaining more realistic surface coverages, the model should also account for the effects of the lack of an alternative nucleation site during accumulation of growth species on the top terrace. It results in an increased probability for incorporation of growth species at the step edges of the top terrace. A smaller effective Schwoebel parameter a on the top surface can be used to model this effect. By causing a slower accumulation of growth species on the upper terrace it will yield a smaller actual surface coverage during nucleation of new terraces.

VII. CONCLUSIONS

The work presented in the previous chapters leads to a number of conclusions. First of all, we have given direct experimental evidence that the formation of growth pyramids on the (111) facet is due to the presence of dislocations. These dislocations can yield spiral as well as concentric step edge patterns, depending on the orientation of the dislocation's Burgers vector. Secondly, the step edge morphology of the CVD grown layers clearly shows that diffusion of the growth species over the terrace does not limit the growth rate. For the CVD experiments described here, the morphology of the observed structures is completely determined by the dependence of the growth rate on the step edge orientation. The surface structures studied in this paper may serve as a useful template for investigating the importance of surface diffusion for other growth conditions. This has been demonstrated in Sec. IV, which describes how MBE overgrowth affects the surface morphology. The results confirm the strong influence of surface diffusion during MBE growth.

Finally, we have deduced that adatoms approaching a step edge from the upper terrace have a slightly larger probability of sticking to that step edge than adatoms approaching from the lower terrace. This conclusion has been obtained by comparing the morphology of the MBE layer on the pyramid's side planes with simulation results.

ACKNOWLEDGMENTS

The authors would like to thank I. Nieuwlaat for making the hemispheres, A. van den Bogaard and E. J. G. Goudena for performing the CVD growth, and B. G. M. de Lange and K. Werner for the MBE growth.

[1] J. G. E. Gardeniers, Ph.D. thesis, University of Nijmegen, 1990.
[2] J. Nishizawa, T. Terasaki, and M. Shimbo, J. Cryst. Growth **17**, 241 (1972).
[3] M. Shimbo, J. Nishizawa, and T. Terasaki, J. Cryst. Growth **23**, 267 (1974).
[4] D. Käss, and H. Strunk, Thin Solid Films **81**, L101 (1981).
[5] J. G. E. Gardeniers, W. E. J. R. Maas, R. Z. C. van Meerten, and L. J. Giling, J. Cryst. Growth **96**, 821 (1989).
[6] I. Sunagawa, K. Tsukamoto, and I. Yashuda, in *Materials Science of the Earth's Interior*, edited by I. Sunagawa (Terra, Tokyo, 1984), p. 331.
[7] W. J. P. van Enckevort, J. Cryst. Growth **119**, 177 (1992).
[8] J. J. Schermer and L. J. Giling, J. Appl. Phys. **78**, 2376 (1995).
[9] T. J. Kreutz, R. E. Clausing, L. Heatherly, R. J. Warmack, T. Thundat, C. S. Feigerle, and K. Wandelt, Phys. Rev. B **51**, 14 554 (1995).
[10] B. Schwartz and H. Robbins, J. Electrochem. Soc. **123**, 1903 (1976).
[11] H. G. van Bueren, *Imperfections in Crystals* (North-Holland, Amsterdam, 1961).
[12] H. Bethge, Phys. Status Solidi **2**, 775 (1962).
[13] E. Bauser and H. Strunk, J. Cryst. Growth **51**, 362 (1981).
[14] E. Bauser and H. Strunk, Thin Solid Films **93**, 185 (1982).
[15] E. Bauser and H. Strunk, J. Cryst. Growth **69**, 561 (1984).
[16] F. Allen and E. Kasper, in *Silicon-Molecular Beam Epitaxy*, edited by E. Kasper and J. C. Bean (CRC Press, Boca Raton, Florida, 1988), Vol. 1.
[17] R. L. Schwoebel and E. J. Shipsey, J. Appl. Phys. **37**, 3682 (1966).